



Photoacoustic elasto-viscography and optical coherence microscopy for multi-parametric *ex vivo* brain imaging

FEN YANG, WENGUO DING, XINLEI FU, WEI CHEN, AND JIANBO TANG* 

Department of Biomedical Engineering, Guangdong Provincial Key Laboratory of Advanced Biomaterials, Southern University of Science and Technology, Shenzhen, Guangdong 518055, China

*tangjb@sustech.edu.cn

Abstract: Optical coherence microscopy (OCM) has shown the importance of imaging *ex vivo* brain slices at the microscopic level for a better understanding of the disease pathology and mechanism. However, the current OCM-based techniques are mainly limited to providing the tissue's optical properties, such as the attenuation coefficient, scattering coefficient, and cell architecture. Imaging the tissue's mechanical properties, including the elasticity and viscosity, in addition to the optical properties, to provide a comprehensive multi-parametric assessment of the sample has remained a challenge. Here, we present an integrated photoacoustic elasto-viscography (PAEV) and OCM imaging system to measure the sample's optical absorption coefficient, attenuation coefficient, and mechanical properties, including elasticity and viscosity. The obtained mechanical and optical properties were consistent with anatomical features observed in the PAEV and OCM images. The elasticity and viscosity maps showed rich variations of microstructural mechanical properties of mice brain. In the reconstructed elasto-viscogram of brain slices, greater elasticity, and lower viscosity were observed in white matter than in gray matter. With the ability to provide multi-parametric properties of the sample, the PAEV-OCM system holds the potential for a more comprehensive study of brain disease pathology.

© 2023 Optica Publishing Group under the terms of the [Optica Open Access Publishing Agreement](#)

1. Introduction

The investigation of the brain anatomy, functionality and disorders highly depends on the availability of bioimaging tools capable of high-resolution large-scale observations with specific contrast [1]. Optical imaging technologies such as optical coherence tomography (OCT) have been playing an important role in neuroanatomy and brain research due to its microscale resolution and millimetre-to-centimetre imaging range [2–7]. However, such imaging techniques have been mainly limited to exploring optical properties of brain tissues. The mechanical properties of brain tissue, such as the elasticity and viscosity are highly correlated to neurodevelopment and neurological disorders, and scarcely investigated with the high-resolution optical imaging modalities.

Recently, it has been recognized that the mechanical properties are important indicators of brain pathologies such as neurodegenerative diseases [8,9]. For brain tissue, viscoelasticity is typically determined by different cell types, their density, mobility, as well as the interaction with extracellular matrix [10]. These variables differ in distinct brain regions in healthy brain and even more significant under pathological conditions. The variations may be reflected in the viscoelastic parameters of brain tissue [11–13]. Therefore, specific changes in brain viscoelasticity can be considered as a potential indicator for diagnosis and prognosis of neuropathological diseases.

A range of elastography techniques have been developed to explore the mechanical properties of brain tissue [14]. Most commonly, a mechanical load is applied to brain tissue and elasticity and/or viscosity is determined by detecting the resulting tissue deformation or the propagation

speed of shear wave. Traditional elastography techniques such as magnetic resonance elastography (MRE) [15,16] and ultrasound elastography (USE) [12,17] have extensively investigated brain viscoelasticity both in small animals and humans. Although such techniques can measure the elasticity over a larger size, their limited spatial resolution precludes detailed mapping of the microstructural viscoelasticity of the brain. With high spatial resolution, atomic force microscopy (AFM) has been used to measure the elastic modulus of the brain subregion such as hippocampal subregions with cellular- or subcellular-scale resolution [18,19]. However, AFM involves nanoindentation, and thus it is invasive and perturbative where the measurement itself may elicit responses of materials. In addition, this technique works typically in small sample, and cannot provide an elasticity map of the whole brain. Therefore, studying brain biomechanics at a microscopic resolution and centimeter-scale volumetric coverage has remained a challenge with existing elastography techniques.

As a hybrid imaging modality, photoacoustic (PA) imaging detects either endogenous or exogenous contrast-induced ultrasound signals through light absorption [20,21]. The unique advantage of scalable spatial resolutions and imaging depths makes PA imaging attractive for various applications, ranging from imaging of nanometre-scale mitochondria to centimetre-level organ in deep tissue. There have been several studies to acquire label-free histology-like PA image of mouse brains with micrometer-resolution [22,23]. In such studies, a single characteristic PA intensity is extracted to visualize the optical absorption magnitude. However, as a laser-induced mechanical wave, PA response potentially carries valuable information about tissue's mechanical features beyond the conventional absorption properties [24–26]. The underlying physics of PAs mechanism—thermoelastic expansion—suggests that the PA temporal response characteristics may be dictated by material's elastic properties.

We have previously proposed a PA method to calculate the elasticity and viscosity parameters simultaneously by exploring the time or phase characteristics of PA response [27–30]. The method has realized multi-scale viscoelastic mappings ranging from cell to organ, and also been demonstrated in pathology applications, such as breast cancer, liver fibrosis and atherosclerotic plaque assessments [31–34]. Here, we extend the capability of the method to brain studies, and develop a PA elasto-viscography (PAEV) and optical coherence microscopy (OCM) imaging system to measure the mechanical elasticity and viscosity moduli and optical attenuation of brain tissues with microscopic resolution. Using freshly resected mice brain tissue slices, rich microstructural biomechanics distributions were observed from the reconstructed elasticity and viscosity maps. Then, in the serial PA elasto-viscogram of brain specimens, distinct brain regions can be clearly identified based on the elastic and viscous moduli variations due to their differences in structure composition and organization. Finally, the PAEV results were further registered and interpreted with OCM, and high correlation in their spatial feature patterns was observed.

2. Methods and materials

2.1. Principle of photoacoustic detection-based elasticity and viscosity measurements

Figure 1(a) shows the generation of photoacoustic (PA) wave, where pulsed optical excitation leads to acoustic emission when sample absorbs the optical energy and undergoes a consequent thermoelastic expansion. The thermoelastic deformation sends out an acoustic wave from the target. In a linear and isotropic material, the PA displacement field $u(r, z, t)$ caused by optical absorption-induced thermoelastic expansion can be described as [28,30,35]

$$\rho \frac{\partial^2 u(r, z, t)}{\partial t^2} - \left(E + \eta \frac{\partial}{\partial t} \right) \nabla^2 u(r, z, t) = \mu_\alpha \mu_{\text{att}} \Gamma I_0 f(t) \exp \left(-\mu_{\text{att}} z - \frac{r^2}{R^2} \right). \quad (1)$$

Here, ρ is the density, E is the elastic modulus, η is the viscosity coefficient, μ_α and μ_{att} are the optical absorption and optical attenuation coefficients, respectively, Γ is the Grueneisen

parameter, I_0 is the laser fluence at the sample surface, $f(t)$ is the temporal dependence of laser pulse that can be approximated δ -distribution, R is the waist radius of the Gaussian beam, and r and z are the radial and axial coordinates, respectively. To simplify the modelling, a surface excitation model of PA point source is considered. The solution of the surface displacement in the transient state follows [36],

$$u(t) = \frac{\sqrt{\pi}}{2} \frac{\mu_a}{\mu_{att}} \frac{\Gamma I_0}{E} \frac{\left(\frac{\sqrt{E/\rho}}{R}\right) t}{\left(\frac{\sqrt{E/\rho}}{R}\right)^2 t^2 + \frac{2\eta}{\rho R^2} t + 1}, \quad (2)$$

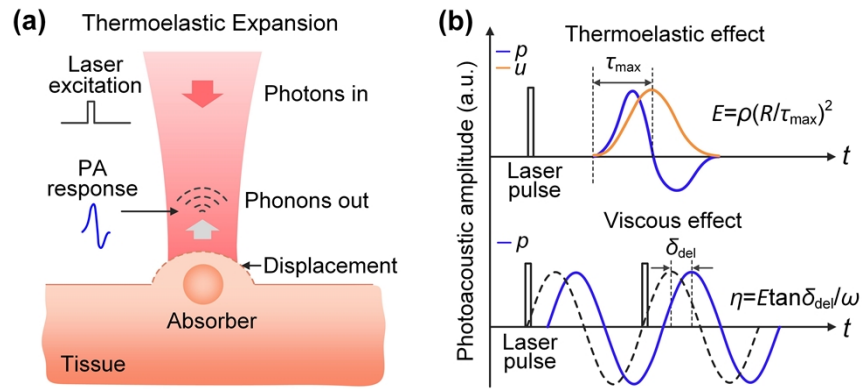


Fig. 1. Principle of photoacoustic elasto-viscography. (a) Laser-induced thermoelastic displacement and subsequent PA response based on the optical absorption-induced thermoelastic expansion. (b) Elasticity and viscosity estimations from the measurements of the rise time and phase delay of PA response.

Equation (2) indicates that the transient temporal response feature of PA displacement is related to the mechanical parameters of the material. As shown in Fig. 1(b) (top), the PA displacement initially increases upon laser irradiation, and reaches a maximum at

$$\tau_{max} = \frac{R}{\sqrt{E/\rho}}. \quad (3)$$

The rise time τ_{max} , i.e., the time-to-peak displacement, is inversely proportional to the elastic modulus. As the expansion-induced displacement is the origin of resulting PA pressure, their relationship is described as $p(t) = -\rho c \partial u(t) / \partial t$, where $p(t)$ is the PA pressure and c is the sound speed [37,38]. As shown in Fig. 1(b) (top), the expansion of sample corresponds to the PA compression wave, and contraction corresponds to the PA rarefaction wave. Therefore, the elasticity E can be estimated by extracting the rise time of PA-induced displacement.

Meanwhile, periodic light excitation leads to cyclical temperature variation in local region and induces a thermal stress, generating a periodic PA strain that has the same frequency with laser excitation [39]. Due to the damping effect caused by tissue viscosity, tissue does not instantaneously respond but gradually deforms as governed by its characteristic relaxation creep [40]. As shown in Fig. 1(b) (bottom), it means that the PA strain responds to laser stimulus with a characteristic phase delay. According to the rheological Kelvin–Voigt model, the relationship

between the phase delay δ_{del} and the viscosity η can be expressed as [27,39]

$$\delta_{\text{del}} = \arctan(\eta\omega/E), \quad (4)$$

where ω is the laser modulation frequency. From Eq. (4), the viscosity parameter η of the sample can be estimated by measuring the PA phase delay δ_{del} .

2.2. PAEV and OCM imaging system

Figure 2 shows a schematic of the developed integrated PAEV and OCM imaging system. The PAEV system used a 1064 nm nanosecond laser (YDFLP-E-20-M7, JPT Opto-Electronics) to generate laser pulses with a 30 ns pulse width and 100 kHz pulse repetition rate. The laser beam was first spatially filtered and expanded by a pair of lenses ($f_1 = 30$ mm; $f_2 = 100$ mm, Thorlabs) and a 50 μm high-energy pinhole. A small portion of the beam was reflected to a photodiode for pulse-to-pulse fluctuation energy compensation. The collimated and expanded beam was then focused using an objective lens (PAL-5-NIR, OptoSigma) with a numerical aperture of 0.15 to illuminate the specimen for photoacoustic excitation. The excited photoacoustic signals were detected in transmission mode by an ultrasonic transducer with a center frequency of 1 MHz (50% –6 dB bandwidth, Olympus). The detected signals were amplified by a low-noise amplifier (LNA-650, RF BAY). To simultaneously obtain the PA rise time and phase delay, the PA signals were transferred to a 250 MS/s data acquisition card (PCIe-8912, ART Technology) and to a lock-in detector (OE2031, SYSU Scientific Instruments), respectively. The lateral resolution of the PAEV system was evaluated by imaging a sharp edge of a surgical blade, as shown in the inset. The edge spread function (ESF) was measured along the line across the agar background and sharp edge of the blade. Taking the derivative of the ESF yields the line spread function (LSF). The lateral resolution, defined as the full width at half maximum (FWHM) of the LSF, was estimated to be 19.8 μm .

The OCM system utilized a superluminescent diode (SLD) with a center wavelength of 1310 nm and a bandwidth of 170 nm as a light source. In the OCT engine, 90% of the light power was sent to the sample, while 10% of the light power was sent to the reference mirror. In both arms, the light was collimated by a collimator. In the sample arm, the collimated beam was reflected by a dichroic mirror and then focused onto the sample using an objective lens. The backscattered light from the sample and light reflected from the reference mirror were then combined by the fiber coupler and delivered to the spectrometer. In the spectrometer, light is collimated by a lens, dispersed by a diffraction grating (Wasatch Photonics, Inc., UT, USA), focused by another lens, and detected by a InGaAs line scan camera (GL2048L, Sensors Unlimited, Inc., NJ, USA) with a sampling rate of 76,000 A-lines/s. The interferogram was recorded by a data acquisition board (PCIe-1433, National Instruments, Corp., TX, USA). The PAEV and OCM subsystems shared a two-dimensional (2D) galvanometer scanning. For large-scale lateral translation of the sample, two additional motorized linear stages were also incorporated. The system control was implemented using LabVIEW programming.

2.3. Tissue sample preparation

The brain was extracted from adult C57BL/6 wide type mice, and harvested immediately after each mouse was sacrificed. The brain was fixed in 3.7% formalin solution at room temperature for 2 days. Afterwards, the brain was embedded in 4% agarose as a block specimen and then sectioned by a home-made vibratome into thin sections (200 μm thick). All experimental animal procedures were carried out in conformity with a laboratory animal protocol approved by the Animal Studies Committee of Southern University of Science and Technology.

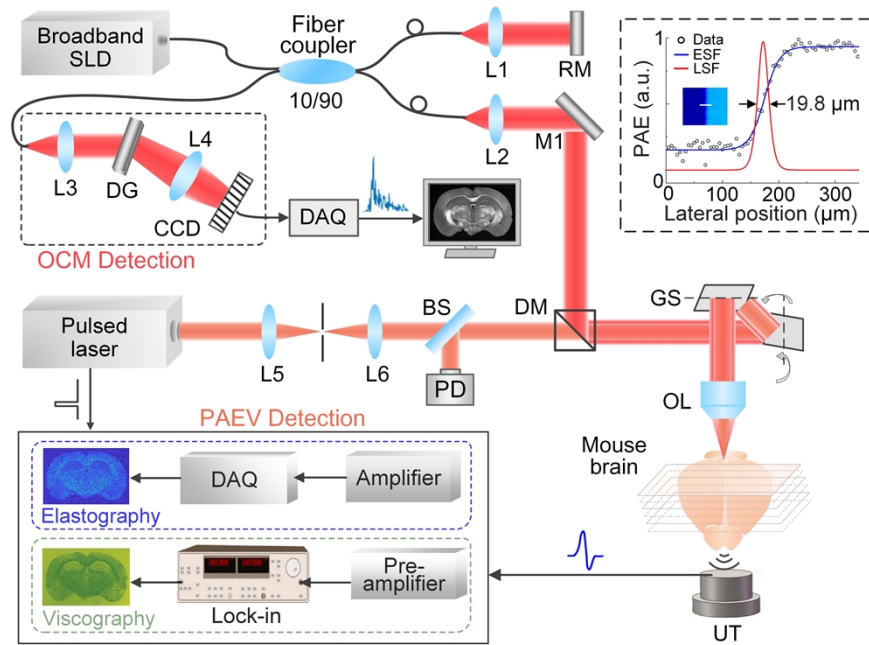


Fig. 2. Schematic of the PAEV and OCM imaging system. For the PAEV module: the laser excitation beams were focused to the sample in a transmission-mode PA microscopy configuration. The OCM module is a spectral domain-optical coherence tomography (SD-OCT) with a broadband superluminescent diode. The two subsystems were combined in free space with the OCT sample arm beam. BS, beam splitter; PD, photodiode; DM, dichroic mirror; GS, galvanometric scanner; OL, objective lens; UT, ultrasound transducer; Amp, amplifier; Pre-amp, pre-amplifier; SLD, super luminescent diode; L1-L6, lens; M1, M2, mirror; DG, diffraction grating, DAQ, data acquisition card. The inset shows the lateral resolution of the PAEV system.

2.4. Data analysis and image reconstruction

Raw PA data for each pixel were acquired. PA signals were bandpass-filtered to remove noise outside the transducer's bandwidth. The maximum intensity projection (MIP) of the PA signals was computed to construct a conventional *en-face* (2D) PA image (i.e., optical absorption) via a 2D raster scanning. For the acquisition of rise time for elasticity estimation, firstly, raw PA signals of target sample were acquired. Subsequently, a background signal was also acquired without laser excitation of the target. The background signal contains the electronic noise of the laser, transducer, and digitizer. Thirdly, the background signal was subtracted from the acquired raw PA signals to obtain the true temporal PA profiles of the target. Fourthly, the PA surface displacement was obtained through the time integration of the time-domain PA signal. Fifthly, the rise time τ_{\max} was computed by $\tau_{\max} = (\tau_2 - \tau_1)$, where the time τ_2 and τ_1 was recorded at peak displacement and zero displacement time point, respectively. Then, the resultant elasticity magnitude was calculated according to Eq. (3) to obtain an *en-face* PA elasticity image. For the acquisition of phase delay for viscosity estimation, firstly, the PA phase of a pure elastic solid was collected to obtain the system's fixed phase delay δ_s caused by the time-of-flight of PA wave propagating between the sample surface (i.e., PA generation position) and transducer. Subsequently, the raw PA phase δ of target sample was collected. Thirdly, the desired viscoelasticity-related phase delay δ_{del} of the target sample was computed by $\delta_{\text{del}} = (\delta - \delta_s)$. Then, the *en-face* PA viscosity image was obtained by the extracted phase delay δ_{del} for each pixel according to Eqs. (3) and (4).

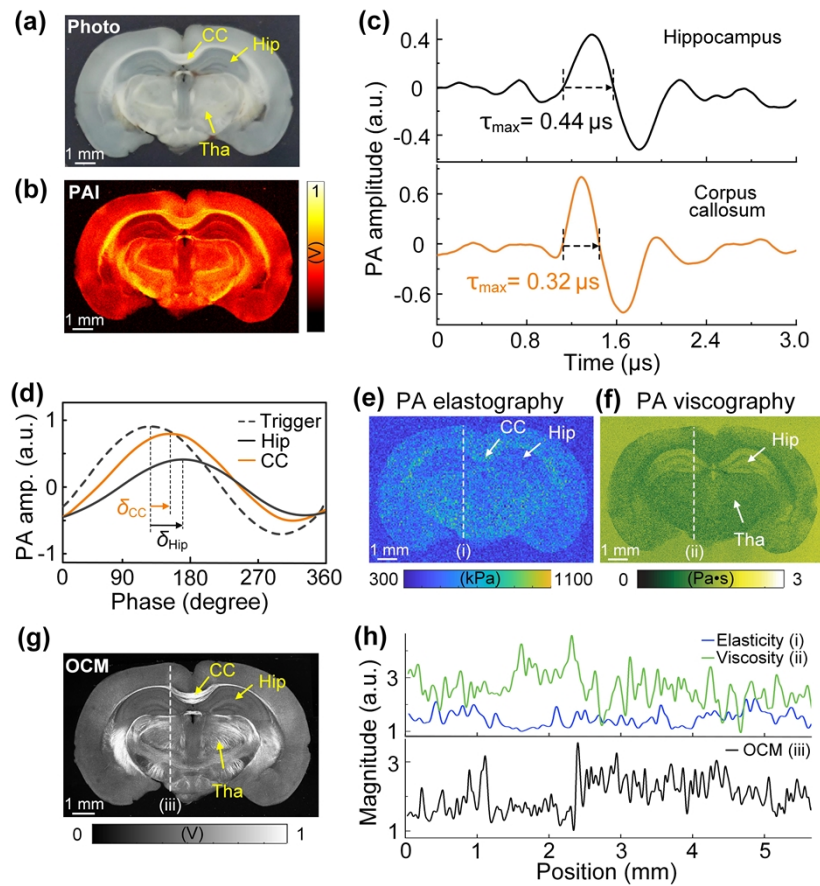


Fig. 3. PAEV and OCM image of a coronal brain section. (a) The photograph of a mouse brain slice. CC, corpus callosum; Hip, hippocampus; tha, thalamus. (b) The conventional structural PA image (PAI). (c) A representative time-domain PA profile of hippocampus and corpus callosum. (d) The phase delay of PA response with respect to the laser stimulus for hippocampus (δ_{Hip}) and corpus callosum (δ_{CC}). (e)–(g) The corresponding PA elastography image (e), PA viscography image (f), and OCM image (g) of a mouse brain slice. (h) The elasticity, viscosity, and optical reflectivity distributions along the white dashed lines (i)–(iii) in (e)–(g), respectively.

The *en-face* OCM reflectivity image was calculated by the maximum intensity projection (MIP) along the axial direction of OCM data. We used an exponential decay model combined with the axial point spread function of the OCM system to extract the attenuation coefficient of the tissue [41], which includes the scattering coefficient and back-scattering coefficient. Light absorption was ignored due to its small contribution in the near-infrared spectral range. We fitted the measured OCM profile using a nonlinear optimization.

2.5. Statistical analysis

Statistical analyses were performed on the regional comparison of brain elasticity and viscosity values using Student's *t*-test (GraphPad Prism 6.0). $P < 0.05$ was considered significant. Data were presented as mean \pm s.d. Pearson correlation analysis was used for comparing the PAEV and OCM data.

2.6. PAEV and OCM imaging of a coronal mouse brain section

The proof-of-concept of the PAEV method on synthetic phantom sample has been reported in our previous studies (Refs. 28,32,36). To validate the performance of PAEV for brain tissue imaging, we imaged a coronal brain slice obtained from a formalin-fixed, agarose-embedded block of mouse brain without additional staining procedures [Fig. 3(a)]. The conventional PA image (PAI) based on the optical absorption contrast was shown in Fig. 3(b), which shows the overall optical absorption architecture of the brain slice. Figure 3(c) shows a representative temporal PA profile of hippocampus and corpus callosum. The two structures exhibited a significant difference in the PA rise time, which helps provide the capability of mapping elasticity distribution. Figure 3(d) shows the corresponding PA phase delay of hippocampus and corpus callosum with respect to the laser stimulus. The variation in the PA phase delay potentially facilitates the identification of the two brain structure types based on their underlying viscous properties. As shown in Fig. 3(e), the elasticity of the coronal brain slice was reconstructed by the corresponding PA rise time. While calculating the PA elastic modulus according to Eq. (3), the material density is 1000 kg/m^3 and the laser spot radius is equal to $10 \text{ }\mu\text{m}$ measured by the PA system's lateral resolution. Different features such as cerebral cortex, corpus callosum, and hippocampus of the brain section can be observed in the PA elastogram [Fig. 3(e)]. In particular, the corpus callosum and hippocampus was clearly visualized due to their large difference in elasticity contrast. More specifically, the corpus callosum region with rich nerve fibers or fiber bundles exhibited a larger elasticity magnitude than hippocampus because fiber is typically stiffer, which is consistent with previous studies [11,12,24]. We emphasize that the different physical nature of high-frequency PA elastic modulus and the often-used low-frequency Young's modulus leads to a large difference in their values, as reported in many publications [28,42–44].

From the measured PA phase delay, Fig. 3(f) further presents the viscosity map of the coronal brain slice. Features such as hippocampus and thalamus can be clearly distinguished based on their viscosity contrasts. The hippocampus has the highest viscosity magnitude because the gray matter region behaves a weak actin crosslink and axonal organization due to poor myelinated axons [15,45]. Note that the PA elastography image [Fig. 3(e)] is relatively blurry compared to the PA viscography image [Fig. 3(f)]. The blurring-like visualization is actually a performance of relatively low elasticity contrast or low precision of elasticity calculation, which potentially originates from the narrow bandwidth of ultrasonic transducer used in this work [28,36]. In contrast, PA viscography image shows relatively superior performance, attributed to high-sensitivity phase delay measurement with lock-in technique. Also note that the minor difference in the viscosity values of brain measured with PAEV and conventional MRE reported in previous study is mainly due to the weak frequency dependence of the viscosity, which interprets the attribution of the strong frequency (ω) to loss modulus ($\eta\omega$) [46].

To validate the capability of mapping microstructural mechanical distributions of PAMV modality, we use optical coherence microscopy (OCM) as a reference for anatomical architecture. As shown in Fig. 3(g), the OCM image reveals finer structural details of coronal brain slice. Similar spatial patterns can be observed in both the PA elasto-viscograms and OCM image. Note that the microstructural feature rendered with PA elasto-viscograms appeared blurry due to their inferior spatial resolution compared to OCM image. To highlight the different feature distributions of brain tissue, Fig. 3(h) shows the line profiles of elasticity, viscosity, and optical reflectivity metrics acquired along the white dashed lines (i)–(iii) in Figs. 3(e)–(g), respectively. The magnitudes of the three parameters presented in Fig. 3(h) were normalized by minimum magnitude for each line profile, which shows similar spatial distribution. In addition, the differences in the relative elasticity-, viscosity-, and optical reflectivity-based contrasts demonstrate that PAEV can provide unique tissue information different from optical properties.

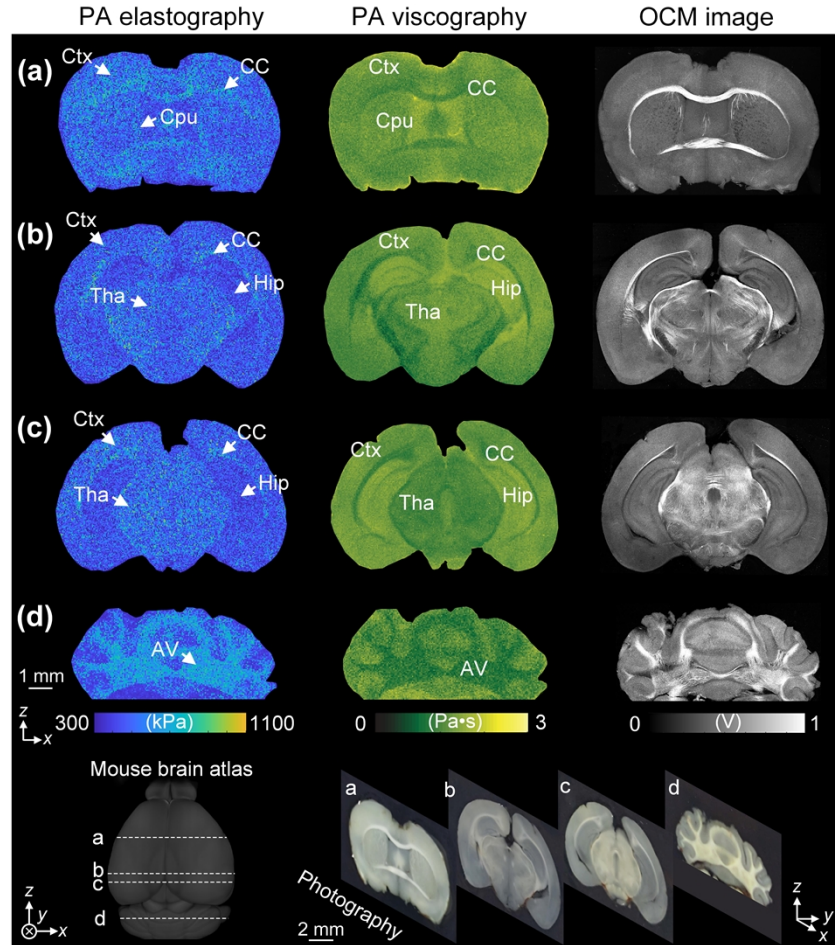


Fig. 4. PAEV and OCM imaging of different brain sections. (a)–(d) PA elastography image (left column), PA viscography image (middle column), and OCM reflectivity image (right column) of four coronal sections. The left bottom inset shows the corresponding positions of the four coronal sections. The right bottom inset shows the photographs of the four coronal sections. Ctx, cerebral cortex; CC, corpus callosum; Cpu, caudate putamen; Hip, hippocampus; Tha, thalamus; AV, arbor vitae.

2.7. PAEV and OCM imaging of different brain sections

Figure 4(a)–(d) presents the PA elastography images (left column) and PA viscography images (middle column), and OCM reflectivity images (right column) of four coronal sections. The coronal sections' corresponding positions were labeled in a three-dimensional (3D) mouse brain model with the white dashed lines, and the slices' photographs were shown in the right bottom figure. As indicated on the PA elastography image (left column), six region of interest (ROI) structures, including cerebral cortex (Ctx), corpus callosum (CC), caudate putamen (Cpu), hippocampus (Hip), thalamus (Tha), and arbor vitae (AV), can be observed from the measured elasticity value. As expected, the nerve fibers- or fiber tracts-rich structures such as corpus callosum and arbor vitae exhibit high elasticity contrasts on the sections [6,22,47]. In the PA viscography image (middle column), the six region of interest (ROI) features could also be identified with a better contrast resulting from highly sensitive lock-in detection. The cerebral

cortex and hippocampus regions exhibit bright green in the pseudocolor map. In contrast, the corpus callosum and arbor vitae regions exhibit dark green due to weak viscous effect from a rich axonal crosslink [15,45]. A strong correlation of the spatial distributions of different brain features could be observed between the PAEV and OCM results. For example, in the OCM reflectivity image (right column), the bright contrasts of the corpus callosum (CC) and arbor vitae (AV) implicate relatively high fiber density [47,48], which corresponds to high elasticity and low viscosity values; the dark contrast (i.e., lower reflectivity signal) in the hippocampus (Hip) indicates relatively low fiber density, corresponding to low elasticity and high viscosity values. The results demonstrated that the PAEV can be used for interrogating biomechanical properties of the brain, which allows exploring biomechanics changes of these structures under different conditions, such as early or late stage of diseases.

2.8. PAEV measurements for different brain regions

To characterize the variations of elasticity and viscosity across brain regions, we analyzed the PAEV measurements and compared them with OCM measurement as well, as shown in Fig. 5. Higher elasticity (i.e., stiffer) was observed in the two white matter structures (the corpus callosum and arbor vitae) with mean elasticity $E = 832$ kPa compared with the three gray matter structures (the cortex, hippocampus, and thalamus) with mean elasticity $E = 593$ kPa, with a significance level of $P < 0.001$, as shown in Fig. 5(a). Consistently, the viscosity also yielded statistically significant differences ($P < 0.001$) between the two white matters ($\eta = 0.76$ Pa•s) and the gray matter regions ($\eta = 1.08$ Pa•s), as shown in Fig. 5(b). We further analyzed the elasticity and viscosity values obtained from three to five brain section specimen over three mice, as shown in Fig. 5(c). As expected, in the five brain regions, the mean elasticity and viscosity values are distinct and their difference are significant.

We further compared the PAEV metrics and the OCM measurements. Figure 5(d) shows the elasticity- and viscosity-based contrasts derived from PAEV images and optical attenuation coefficient-based contrast obtained from OCM image of the cortex, hippocampus, and arbor vitae structures, where the contrasts were normalized to the magnitudes of cortex. The estimated elasticity contrast feature from PA elastography image shows analogous trend to the optical attenuation contrast from OCM image, suggesting that the two parameters show a positive correlation. It can be interpreted that, for instance, the fiber component of white matter tract typically behaves stiff in mechanical properties and high optical attenuation in optical properties. In contrast, the obtained viscosity contrast from PA viscography image was negatively correlated with the optical attenuation contrast. This can be attributed to that, as exemplified by the white matter structure, tight organization of myelinated fiber contributes to flexibility and photon attenuation.

To quantify the correlations, we compared the elasticity and viscosity distributions in the PA elastography and viscography images with the optical attenuation coefficient of the corresponding position in the OCM image. From Fig. 5(e), a comparison between the averaged elasticity and optical attenuation of 50 ROIs in the four brain sections in Fig. 4 reveals a positive correlation with a correlation coefficient of 0.79 ($R^2 = 0.74$, $P < 0.0001$). Similarly, as shown in Fig. 5(f), the point-to-point scatter plot shows that the viscosity index has a negative correlation coefficient of -0.42 ($R^2 = 0.40$, $P < 0.0001$) to the optical attenuation. The weak linear relationship can be attributed to the inconsistent spatial resolution ability for finer structure of brain tissue between PAV and OCM. These results indicate the ability of PAEV technique in investigating biomechanical properties of brain.

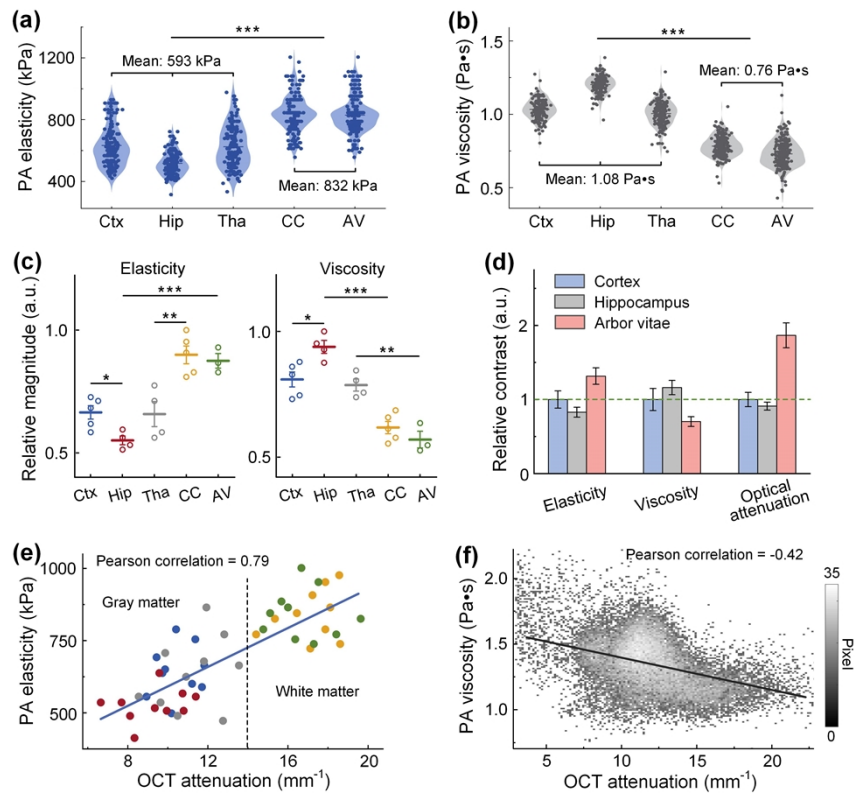


Fig. 5. PAEV measurements for different brain regions. (a), (b) Violin plots comparing PA elasticity (a) and PA viscosity (b) levels of different brain regions. Ctx, cerebral cortex; Hip, hippocampus; Tha, thalamus; CC, corpus callosum; AV, arbor vitae. (c) Statistics of the regional elasticity and viscosity from three to five brain section specimen. Data are presented as mean \pm s.d. (d) The relative contrast of elasticity, viscosity, and optical attenuation parameters of cortex, hippocampus, and arbor vitae structures. (e) Comparison of PA elasticity metric and optical attenuation feature for the five brain regions. (f) Point-to-point scatter plot comparing the viscosity index with optical attenuation measurement obtained from the third brain section image (i.e., third row) in Fig. 4(c).

3. Discussion and conclusions

This work shows that the PAEV is able to provide high-resolution, high-sensitivity mapping of viscoelastic parameters of the brain tissue. In combination with the OCM, the PAEV-OCM technique would be a useful tool to quantify tissues' mechanical properties in addition to optical properties, which would play an important role in studying the disease pathology. Different from conventional PA imaging, PAEV utilizes the time and phase characteristics of PA response to extract unique tissue's viscoelastic information. As a PA-based functional extension, PAEV opens new avenues for conventional PA imaging by adding dimensions to the absorption contrast, expanding specificity. Additionally, the technique can be easily integrated into existing PA imaging platform to allow for simultaneous visualization of brain morphology, micromechanics, and functionality traits.

Efforts are needed to correlate the PA-deduced elastic modulus to often-used Young's modulus for a complete description of the stiffness or compliance of the tissue. The correlation is believed to result from the common dependence of bulk or longitudinal modulus and Young's modulus on underlying biophysical factors and characteristics of biological samples [42–44,49,50]. Although the relationship between them is not straightforward and sample dependent, establishing an empirical correlation may be an alternative to acquire a reliable correlation through careful calibration and in a sample-dependent manner [44,50]. For instance, the combination of the elastographic extension of well-established OCM system, i.e., optical coherence elastography (OCE) and PAEV introduced in this work, enables an establishment of the quantitative relationship between the PAEV-derived bulk modulus and OCE-obtained Young's modulus based on the same sample, allowing us to completely map the elastic moduli of brain tissue.

In the PAEV experiments, a laser repetition rate of 100 kHz was selected as a trade-off of ensuring a sufficient time interval between consecutive mechanical responses of the material under investigation and high-frequency excitation for fast data acquisition. Although the laser pulse excitation of 30 ns is longer than that used in most PA studies, thermal confinement is still satisfied to obtain optimized conversion efficiency from light absorption to ultrasound emission based on the thermoelastic expansion effect. Note that the PAEV-based elasticity and viscosity derives from the detected PA signal, the PA signal at or below noise level would lead to a low accuracy of viscoelastic estimations. Therefore, enhancing the induction and detection of PA signal is an important aspect that need to be taken into consideration. An ultrasonic transducer with 1 MHz center frequency was selected due to its high detection sensitivity to enhance the signal-to-noise ratio (SNR). Although the axial resolution was sacrificed, the en-face viscoelastic properties mappings that this work focused on would not be affected.

In this work, because the brain slice obtained by a microtome has a flat surface, an undesired phase deviation caused by uneven surface would not be generated. Although for tissue sample with a rough surface in *in vivo* or clinical application, a phase correction algorithm combining a sound propagation model with the depth-resolved structural information obtained from conventional PA tomography or from OCT can be used to achieve pure viscoelasticity-induced phase delay for accurate viscosity measurement. In addition, in our PAEV system, the stability of excitation source emission time ensures a same phase zero point, and thus also contributes to a reliable measurement of tissue viscosity-related phase delay.

The PAEV-OCM technique can be improved to a fully automatic serial sectioning and real-time PA elasto-viscography platform by combining with a vibratome and using the reflection mode-based PA detection. In the reflection mode-based configuration, PAEV-OCM system does not require thin slicing of the tissue sample. The serial removal of previously imaged tissue sections will greatly improve the imaging throughput, and thus allows 3D whole mouse brain imaging by stacking slice by slice without complex image registration. In addition, the throughput can also be improved with the combination of a fast laser and fast scanning mechanism in the future. In our current PAEV experiment, with a laser repetition rate of 100 kHz, acquiring an

approximately $1\text{ cm} \times 1\text{ cm}$ image with a $50\text{ }\mu\text{m}$ step size takes about 2 hours. The imaging speed is mainly limited by the time constant of the lock-in detector, and usually the time constant is set at 100 ms to obtain a robust phase delay. In future studies, the lock-in time constant can be reduced by improving the detection sensitivity with a focused ultrasound transducer. Moreover, with a cross-correlation processing algorithm between PA signal and reference signal without employing the lock-in detector device, the imaging speed can be dramatically improved [51–53].

In conclusion, we presented a PAEV method for brain-wide mappings of elastic and viscous parameters with high spatial resolution. We demonstrated the mechano-microscopy capability to map mechanical features of coronal mouse brain section. For validation, we utilized the co-registered PAEV and OCM system to correlate various regions of viscoelastic properties with microstructural morphologies of the brain tissue. The PAEV adds additional mechanical contrast to OCM-based optical property, which provides more comprehensive evaluations of tissue properties for disease study.

Funding. The National Natural Science Foundation of China (62275116, 62220106006); the Natural Science Foundation of Guangdong Province (2022A1515011984); the Shenzhen Science and Technology Innovation Program (20210316161406001); the China Postdoctoral Science Foundation (2022M721483); the Guangdong Provincial Key Laboratory of Advanced Biomaterials (2022B1212010003).

Disclosures. The authors declare no conflicts of interest.

Data Availability. Data underlying the results presented in this paper are not publicly available at this time but may be obtained from the authors upon reasonable request.

References

1. R. C. Craddock, S. Jbabdi, C. G. Yan, J. T. Vogelstein, F. X. Castellanos, A. Di Martino, C. Kelly, K. Heberlein, S. Colcombe, and M. P. Milham, "Imaging human connectomes at the macroscale," *Nat. Methods* **10**(6), 524–539 (2013).
2. K. Amunts, C. Lepage, L. Borgeat, H. Mohlberg, T. Dickscheid, M.-É. Rousseau, S. Bludau, P.-L. Bazin, L. B. Lewis, A.-M. Oros-Peusquens, N. J. Shah, T. Lippert, K. Zilles, and A. C. Evans, "BigBrain: an ultrahigh-resolution 3D human brain model," *Science* **340**(6139), 1472–1475 (2013).
3. T. Ragan, L. R. Kadiri, K. U. Venkataraju, K. Bahlmann, J. Sutin, J. Taranda, I. A. Carreras, Y. Kim, H. S. Seung, and P. Osten, "Serial two-photon tomography for automated ex vivo mouse brain imaging," *Nat. Methods* **9**(3), 255–258 (2012).
4. A. Li, H. Gong, B. Zhang, Q. Wang, C. Yan, J. Wu, Q. Liu, S. Zeng, and Q. Luo, "Micro-optical sectioning tomography to obtain a high-resolution atlas of the mouse brain," *Science* **330**(6009), 1404–1408 (2010).
5. H. Hama, H. Kurokawa, H. Kawano, R. Ando, T. Shimogori, H. Noda, K. Fukami, A. S. Sawano, and A. Miyawaki, "Scale: a chemical approach for fluorescence imaging and reconstruction of transparent mouse brain," *Nat. Neurosci.* **14**(11), 1481–1488 (2011).
6. H. Wang, C. Magnain, R. Wang, J. Dubb, A. Varjabedian, L. S. Tirrell, A. Stevens, J. C. Augustinack, E. Konukoglu, I. Aganj, M. P. Frosch, J. D. Schmahmann, B. Fischl, and D. A. Boas, "As-PSOCT: volumetric microscopic imaging of human brain architecture and connectivity," *NeuroImage* **165**, 56–68 (2018).
7. S. Na, J. J. Russin, L. Lin, X. Yuan, P. Hu, K. B. Jann, L. Yan, K. Maslov, J. Shi, D. J. Wang, C. Y. Liu, and L. V. Wang, "Massively parallel functional photoacoustic computed tomography of the human brain," *Nat. Biomed. Eng.* **6**(5), 584–592 (2021).
8. D. E. Koser, A. J. Thompson, S. K. Foster, A. Dwivedy, E. K. Pillai, G. K. Sheridan, H. Svoboda, M. Viana, L. d. F. Costa, J. Guck, C. E. Holt, and K. Franze, "Mechanosensing is critical for axon growth in the developing brain," *Nat. Neuroscience* **19**(12), 1592–1598 (2016).
9. S. Cheng, E. C. Clarke, and L. E. Bilston, "Rheological properties of the tissues of the central nervous system: A review," *Med. Eng. Phys.* **30**(10), 1318–1337 (2008).
10. L. Chen, W. Li, V. Maybeck, A. Ofenhusser, and H.-J. Krause, "Statistical study of biomechanics of living brain cells during growth and maturation on artificial substrates," *Biomaterials* **106**, 240–249 (2016).
11. J. Weickenmeier, R. de Rooij, S. Budday, P. Steinmann, T. C. Ovaert, and E. Kuhl, "Brain stiffness increases with myelin content," *Acta Biomater.* **42**, 265–272 (2016).
12. E. Macé, I. Cohen, G. Montaldo, R. Miles, M. Fink, and M. Tanter, "In vivo mapping of brain elasticity in small animals using shear wave imaging," *IEEE Trans. Med. Imaging* **30**(3), 550–558 (2011).
13. L. V. iscox, C. L. Johnson, M. D. J. McGarry, H. Marshall, C. W. Ritchie, E. J. R. van Beek, N. Roberts, and J. M. Starr, "Mechanical property alterations across the cerebral cortex due to Alzheimer's disease," *Brain Commun.* **2**(1), fcz049 (2020).
14. N. Leartprapun and S. G. Adie, "Recent advances in optical elastography and emerging opportunities in the basic sciences and translational medicine," *Biomed. Opt. Express* **14**(1), 208–248 (2023).

15. L. V. Hiscox, H. Schwarb, M. D. J. McGarry, and C. L. Johnson, "Aging brain mechanics: progress and promise of magnetic resonance elastography," *NeuroImage* **232**, 117889 (2021).
16. M. C. Murphy, J. Huston, and R. L. Ehman, "MR elastography of the brain and its application in neurological diseases," *NeuroImage* **187**, 176–183 (2019).
17. R. M. S. Sigrist, J. Liao, A. E. Kaffas, M. C. Chammas, and J. K. Willmann, "Ultrasound elastography: review of techniques and clinical applications," *Theranostics* **7**(5), 1303–1329 (2017).
18. A. S. Morr, M. Nowicki, G. Bertalan, R. V. Silva, C. I. Duarte, S. P. Koch, P. B. Sturm, U. Krügel, J. Braun, B. Steiner, J. A. Käs, T. Fuhs, and I. Sack, "Mechanical properties of murine hippocampal subregions investigated by atomic force microscopy and in vivo magnetic resonance elastography," *Sci. Rep.* **12**(1), 16723 (2022).
19. N. Antonovaite, S. V. Beekmans, E. M. Hol, W. J. Wadman, and D. Iannuzzi, "Regional variations in stiffness in live mouse brain tissue determined by depth-controlled indentation mapping," *Sci. Rep.* **8**(1), 12517 (2018).
20. M. Omar, J. Aguirre, and V. Ntziachristos, "Optoacoustic mesoscopy for biomedicine," *Nat. Biomed. Eng.* **3**(5), 354–370 (2019).
21. J. Yao, L. Wang, J. M. Yang, K. I. Maslov, T. T. Wong, L. Li, C. H. Huang, J. Zou, and L. V. Wang, "High-speed label-free functional photoacoustic microscopy of mouse brain in action," *Nat. Methods* **12**(5), 407–410 (2015).
22. T. T. W. Wong, R. Zhang, C. Zhang, H.-C. Hsu, K. I. Maslov, L. Wang, J. Shi, R. Chen, K. K. Shung, Q. Zhou, and L. V. Wang, "Label-free automated three-dimensional imaging of whole organs by microtomy-assisted photoacoustic microscopy," *Nat. Commun.* **8**(1), 1386 (2017).
23. J. W. Baik, H. Kim, M. Son, J. Choi, K. G. Kim, J. H. Baek, Y. H. Park, J. An, H. Y. Choi, S. Y. Ryu, J. Y. Kim, K. Byun, and C. Kim, "Intraoperative label-free photoacoustic histopathology of clinical specimens," *Laser Photonics Rev.* **15**(10), 2100124 (2021).
24. N. Pellegrino, B. R. Ecclestone, D. Dinakaran, F. van Landeghem, P. Fieguth, and P. H. Reza, "Time-domain feature extraction for target specificity in photoacoustic remote sensing microscopy," *Opt. Lett.* **47**(15), 3952–3955 (2022).
25. R. Zhang, F. Gao, X. Feng, S. Liu, R. Ding, and Y. Zheng, "Photoacoustic resonance imaging," *IEEE J. Sel. Top. Quantum Electron.* **25**(1), 1–7 (2019).
26. B. Soroushian, W. M. Whelan, and M. C. Kolios, "Study of laser-induced thermoelastic deformation of native and coagulated ex-vivo bovine liver tissues for estimating their optical and thermomechanical properties," *J. Biomed. Opt.* **15**(6), 065002 (2010).
27. G. Gao, S. Yang, and D. Xing, "Viscoelasticity imaging of biological tissues with phase-resolved photoacoustic measurement," *Opt. Lett.* **36**(17), 3341–3343 (2011).
28. F. Yang, Z. Chen, and D. Xing, "Single-cell photoacoustic microrheology," *IEEE Trans. Med. Imaging* **39**(6), 1791–1800 (2020).
29. Y. Zhao, C. Chen, H. Liu, S. Yang, and D. Xing, "Time-resolved photoacoustic measurement for evaluation of viscoelastic properties of biological tissues," *Appl. Phys. Lett.* **109**(20), 203702 (2016).
30. Y. Yuan, X. Wen, B. Yuan, H. Xin, B. Fang, S. Yang, and K. Xiong, "Photoacoustic remote sensing elastography," *Opt. Lett.* **48**(9), 2321–2324 (2023).
31. Y. Zhao, S. Yang, C. Chen, and D. Xing, "Simultaneous optical absorption and viscoelasticity imaging based on photoacoustic lock-in measurement," *Opt. Lett.* **39**(9), 2565–2568 (2014).
32. Q. Wang, Y. Shi, F. Yang, and S. Yang, "Quantitative photoacoustic elasticity and viscosity imaging for cirrhosis detection," *Appl. Phys. Lett.* **112**(21), 211902 (2018).
33. Y. Zhao, S. Yang, C. Chen, and D. Xing, "Mechanical evaluation of lipid accumulation in atherosclerotic tissues by photoacoustic viscoelasticity imaging," *Opt. Lett.* **41**(19), 4522–4525 (2016).
34. P. Wang, Z. Chen, F. Yang, S. Yang, and D. Xing, "Intravascular tri-modality system: Combined ultrasound, photoacoustic, and elasticity imaging," *Appl. Phys. Lett.* **113**(25), 253701 (2018).
35. T. Wang, T. Pfeiffer, M. Wu, W. Wieser, G. Amenta, W. Draxinger, A. F. van der Steen, R. Huber, and G. van Soest, "Thermo-elastic optical coherence tomography," *Opt. Lett.* **42**(17), 3466–3469 (2017).
36. F. Yang, Z. Chen, and D. Xing, "All-optical noncontact phase-domain photoacoustic elastography," *Opt. Lett.* **46**(19), 5063–5066 (2021).
37. I. G. Calasso, W. Craig, and G. J. Diebold, "Photoacoustic point source," *Phys. Rev. Lett.* **86**(16), 3550–3553 (2001).
38. Z. Ma, N. Ding, Z. Li, K. Zhu, A. Li, Z. Lin, Y. Wang, Y. Zhao, Y. Yu, J. Luan, X. Zhu, and J. Liu, "Spectral interference contrast based non-contact photoacoustic microscopy realized by SDOCT," *Opt. Lett.* **47**(11), 2895–2898 (2022).
39. Y.-C. Fung, *Biomechanics: Mechanical Properties of Living Tissues* (Springer, 2013).
40. T. G. Mason and D. A. Weitz, "Optical measurements of frequency-dependent linear viscoelastic moduli of complex fluids," *Phys. Rev. Lett.* **74**(7), 1250–1253 (1995).
41. J. Yang, I. A. Chen, S. Chang, J. Tang, B. Lee, K. Kılıç, S. Sunil, H. Wang, D. Varadarajan, C. Magnain, S.-C. Chen, I. Costantini, F. Pavone, B. Fischl, and D. A. Boas, "Improving the characterization of *ex vivo* human brain optical properties using high numerical aperture optical coherence tomography by spatially constraining the confocal parameters," *Neurophotonics* **7**(04), 045005 (2020).
42. R. Prevedel, A. Diz-Muñoz, G. Ruocco, and G. Antonacci, "Brillouin microscopy: An emerging tool for mechanobiology," *Nat. Methods* **16**(10), 969–977 (2019).

43. M. Bailey, M. A. Cardinali, N. Correa, S. Caponi, T. Holsgrove, H. Barr, N. Stone, C. P. Winlove, D. Fioretto, and F. Palombo, "Viscoelastic properties of biopolymer hydrogels determined by Brillouin spectroscopy: A probe of tissue micromechanics," *Sci. Adv.* **6**(44), 1937 (2020).
44. G. Scarcelli, W. J. Polacheck, H. T. Nia, K. Patel, A. J. Grodzinsky, R. D. Kamm, and S. H. Yun, "Noncontact three-dimensional mapping of intracellular hydromechanical properties by Brillouin microscopy," *Nat. Methods* **12**(12), 1132–1134 (2015).
45. J. Guo, G. Bertalan, D. Meierhofer, C. Klein, S. Schreyer, B. Steiner, S. Wang, R. V. da Silva, C. I. Duarte, S. Koch, P. B. Sturm, J. Braun, and I. Sack, "Brain maturation is associated with increasing tissue stiffness and decreasing tissue fluidity," *Acta Biomater.* **99**, 433–442 (2019).
46. T. Munder, A. Pfeffer, S. Schreyer, J. Guo, J. Braun, I. Sack, B. Steiner, and C. Klein, "MR elastography detection of early viscoelastic response of the murine hippocampus to amyloid β accumulation and neuronal cell loss due to Alzheimer's disease," *J. Magn. Reson. Imaging* **47**(1), 105–114 (2018).
47. H. Wang, T. Akkin, C. Magnain, R. Wang, J. Dubb, W. J. Kostis, M. A. Yaseen, A. Cramer, S. Sakadžić, and D. Boas, "Polarization sensitive optical coherence microscopy for brain imaging," *Opt. Lett.* **41**(10), 2213–2216 (2016).
48. J. Lefebvre, P. D. Martel, P. Pouliot, H. Girouard, M. Descoteaux, and F. Lesage, "Fully automated dual-resolution serial optical coherence tomography aimed at diffusion MRI validation in whole mouse brains," *Neurophotonics* **5**(04), 1 (2018).
49. Y. S. Ambekar, M. Singh, A. W. Schill, J. Zhang, C. Z. Delgado, B. Khajavi, S. R. Aglyamov, R. H. Finnell, G. Scarcelli, and K. V. Larin, "Multimodal imaging system combining optical coherence tomography and Brillouin microscopy for neural tube imaging," *Opt. Lett.* **47**(6), 1347–1350 (2022).
50. Y. S. Ambekar, M. Singh, J. Zhang, A. Nair, S. R. Aglyamov, G. Scarcelli, and K. V. Larin, "Multimodal quantitative optical elastography of the crystalline lens with optical coherence elastography and Brillouin microscopy," *Biomed. Opt. Express* **11**(4), 2041–2051 (2020).
51. P. Tang, S. Liu, J. Chen, Z. Yuan, B. Xie, J. Zhou, and Z. Tang, "Cross-correlation photothermal optical coherence tomography with high effective resolution," *Opt. Lett.* **42**(23), 4974–4977 (2017).
52. S. Du, Z. Chen, and D. Xing, "Spectral interferometric depth-resolved photoacoustic viscoelasticity imaging," *Opt. Lett.* **46**(7), 1724–1727 (2021).
53. M. H. Salimi, M. Villiger, and N. Tabatabaei, "Transient-mode photothermal optical coherence tomography," *Opt. Lett.* **46**(22), 5703–5706 (2021).